



Reactive oxygen species (ROS) and sensitization to TRAIL-induced apoptosis, in Bayesian network modelling of HeLa cell response to LY303511

Lisa Tucker-Kellogg^{a,b,1}, Yuan Shi^{a,1}, Jacob K. White^{a,c}, Shazib Pervaiz^{a,d,e,*}

^a Computational Systems Biology Programme, Singapore-MIT Alliance, Singapore 117576, Singapore

^b Mechanobiology Institute, National University of Singapore, Singapore 117411, Singapore

^c Department of Electrical Engineering and Computer Science, Massachusetts Institute of Technology, Cambridge, MA 02139, USA

^d Department of Physiology, Yong Loo Lin School of Medicine, The National University of Singapore, Singapore

^e Graduate School of Integrative Sciences and Engineering, National University of Singapore, Singapore 119260, Singapore

ARTICLE INFO

Article history:

Received 29 June 2012

Accepted 30 August 2012

Available online 6 September 2012

Keywords:

Reactive oxygen species

Combination therapy

Systems biology

Cancer apoptosis

Computational models

ABSTRACT

Background: The compound LY303511 (LY30) has been proven to induce production of ROS and to sensitize cancer cells to TRAIL-induced apoptosis, but the mechanisms and mediators of LY30-induced effects are potentially complex. Bayesian networks are a modelling technique for making probabilistic inferences about complex networks of uncertain causality.

Methods: Fluorescent indicators for ROS, reactive nitrogen species (RNS), and free calcium were measured in time-series after LY30 treatment. This “correlative” dataset was used as input for Bayesian modelling to predict the causal dependencies among the measured species. Predictions were compared against a separate “causal” dataset, in which cells had been treated with FeTPPS to scavenge peroxynitrite, EGTA-am to chelate calcium, and Tiron to scavenge $O_2^{\bullet-}$. Finally, cell viability measurements were integrated into an extended model of LY30 effects.

Results: LY30 treatment caused a rapid increase of ROS (measured by DCFDA) as well as a significant increase in RNS and calcium. Bayesian modelling predicted that Ca^{2+} was a partial cause of the ROS induced by short incubations with LY30, and that RNS was strongly responsible for the ROS induced by long incubations with LY30. Validation experiments confirmed the predicted roles of RNS and calcium, and also demonstrated a causal role for $O_2^{\bullet-}$. In cell viability experiments, the additive effects of calcium and peroxynitrite were responsible for 90% of LY30-mediated sensitization to TRAIL-induced apoptosis.

Conclusions: We conclude that LY30 induces interdependent pathways of reactive species and stress signalling, with peroxynitrite and calcium contributing most significantly to apoptosis sensitization.

© 2012 Elsevier Inc. All rights reserved.

1. Introduction

The drug LY303511 (LY30), an inactive analogue of the PI3K inhibitor LY294002 [1,2], has been found to sensitize multiple cancer cell lines to TRAIL- and vincristine-induced apoptosis [3–5]. Sensitization to apoptosis is an important therapeutic objective because many cancers develop resistance to single anti-cancer therapies such as TRAIL [6]. In the cell lines tested, LY30 was observed to induce a significant increase in reactive oxygen species (ROS) production, measured as DCFDA fluorescence. ROS production is important to many pathways of apoptosis sensitization [7], and to the mechanisms of many chemotherapeutic compounds [8,9]. High levels of ROS may promote apoptosis, particularly in

cancer cells that have high metabolic rates and high levels of oxidative stress [10]. Previous work did not establish the origin(s) or the precise nature of the ROS implicated in the death sensitizing activity of LY30.

The ROS category includes oxygen radicals such as superoxide ($O_2^{\bullet-}$) and hydroxyl radical (OH^{\bullet}), and nonradical compounds that are easily converted into radicals, such as peroxynitrite ($ONOO^-$), HOCl, and H_2O_2 . Under physiological conditions, ROS are a natural by-product of the electron transport chain (ETC) [11], but other intracellular mechanisms can produce ROS under normal conditions, such as NADPH oxidase; or under stress, such as the endoplasmic reticulum (ER). In many cases, the ratio of $O_2^{\bullet-}$ to H_2O_2 determines whether ROS will promote or hinder apoptosis [12], but many species can affect cell fate. ROS levels and apoptosis signalling can be regulated by reactive nitrogen species (RNS) and by Ca^{2+} levels [13]. For example, $ONOO^-$ is a member of both the ROS and RNS categories, and it is formed by the rapid reaction of NO with $O_2^{\bullet-}$. $ONOO^-$ is known to induce apoptosis at low levels and trigger necrosis at high levels [14]. In addition, ROS can

* Corresponding author at: Department of Physiology, National University of Singapore, Singapore. Tel.: +65 6516 6602.

E-mail address: Shazib_Pervaiz@nuhs.edu.sg (S. Pervaiz).

¹ These authors contributed equally.

increase Ca^{2+} levels [13], which in turn can stimulate a further increase in ROS production, through RNS-dependent [15,16] and RNS-independent pathways [17]. In sum, the pathways are interconnected.

The causal roles of ROS, RNS, and/or Ca^{2+} , towards each other and towards apoptosis sensitization, are potentially complex. Bayesian probability is a mathematical framework for computing conditional probabilities, such as the probability of an effect given a cause, or more interestingly, the probability of a possible cause given an observed effect. Bayesian networks can use incomplete information for efficient “learning” of causal dependencies between multiple variables in a system [18]. Whether using Bayesian networks or any other formalism, modelling research often constructs models based on a specific *training dataset*, while the predictive accuracy of the model is evaluated using a separate *test dataset*, that has not been used during model-building. Models with incorrect mechanisms can be “overfit” to match their training data, but such models can rarely predict the results in the test dataset. A model that can match both training dataset and test dataset is more likely to simulate a correct mechanism.

In this work, we studied the roles of $\text{O}_2^{\bullet-}$, RNS, and Ca^{2+} , as candidate mediators for the effects of LY30 on ROS production, and on TRAIL-induced apoptosis in HeLa cells. Bayesian network modelling was performed using a training dataset of time-series observations in LY30-treated cells, and validated using a test dataset of time-series observations with scavengers of $\text{O}_2^{\bullet-}$, RNS, or Ca^{2+} . As a second test, the Bayesian network was trained on a dataset of cell viability, and tested on a dataset of combination inhibitor treatments.

2. Materials and methods

2.1. Cells and anti-cancer treatments

HeLa human cervical cancer cell line was purchased from American Type Culture Collection (ATCC, Rockville, MD, USA) and maintained in Dulbecco's Modified Eagle's Medium (DMEM) supplemented with 10% FBS, 1% L-glutamine, and 1% S-penicillin. HeLa cells were plated at 0.125 million cells/well in 24-well plates (and proportionally for other size plates) and grown overnight until 80% confluent.

All treatments with LY30 (Alexis, Switzerland) and TRAIL (Biomol, Plymouth Meeting, PA, USA) used the methods, dosing, and schedules as previously reported [4]. In particular, combination treatments of LY30 and TRAIL involved pre-incubation of cells with 25 μM LY30 for 1 h before addition of 20 ng/ml TRAIL.

2.2. Flow cytometry measurements

After specific treatments, cells were washed with $1 \times$ PBS, and loaded with fluorescent dyes according to manufacturers' recommendations. In particular, cells were incubated for 20 min with fresh CM- H_2DCFDA (DCFDA) at 5 μM , DAF-FM (DAF) at 5 μM , MitoSOX-red (MitoSOX) at 10 μM , or dihydroethidium (DHE) at 5 μM . Then, cells were washed again with $1 \times$ PBS and analysed under flow cytometry. DCFDA and DAF were analysed with excitation wavelength at 488 nm and emission wavelength at 517 nm. Cells with DHE and MitoSOX staining were analysed with excitation wavelength at 400 nm and emission wavelength at 590 nm. For each treatment, at least 10,000 events were obtained. Data were then gated according to side scatter (SS) and forward scatter (FS), to exclude cellular debris. Once set, gates were applied to all samples in the experiment. For quantification, we firstly obtained the average fluorescence intensity of each sample (e.g. $F_{i_measured}$ for sample i), and then normalized it according to the formula $R_i = (F_{i_measured} - F_{unstained}) / (F_{CTL_measured} - F_{unstained})$

where R_i is the normalized level of sample i ; $F_{unstained}$ is the absolute fluorescence from unstained control, and $F_{CTL_measured}$ is the absolute fluorescence from untreated control sample.

2.3. Scavengers, inhibitors, and chelators.

$\text{O}_2^{\bullet-}$ scavenger Tiron (Sigma–Aldrich) was applied at 10 mM to cells 1 h before adding LY30. Ca^{2+} chelator EGTA-am (Life Technologies) was administered at 25 μM to cells 15 min before adding LY30. Peroxynitrite scavenger FeTPPS (Calbiochem, San Diego, CA, USA) was administered to cell samples at concentrations of 50 μM or 100 μM , 1 h before LY30 treatment. SOD-1 (Cu/ZnSOD) inhibitor DDC (Sigma–Aldrich) was applied to cells at concentrations of 200 mM or 400 mM, with 2 h pre-incubation before LY30. Thapsigargin (Life Technologies) was applied at 1 mM. $\text{O}_2^{\bullet-}$ inhibitor Tiron (4,5-dihydroxy-1,3-benzenedisulfonic acid disodium salt, Sigma–Aldrich) was added at 10 mM with 1 h pre-incubation before LY30. Experiments with the H_2O_2 scavenger catalase (C3511 catalase from bovine liver, Sigma–Aldrich) were administered into wells at doses of 2000 units/ml one day before the treatment with LY30. On the second day, cells were changed with fresh media and catalase was added again at the same concentration (2000 units/ml; 4000 units/ml) together with LY30 (25 μM).

2.4. $\text{O}_2^{\bullet-}$ measurement using Lucigenin

HeLa cells were seeded in 100 mm tissue culture plates 24 h before performing the experiment. Cells were washed once with $1 \times$ PBS, and then detached with $1 \times$ trypsin (Trypsin, Hyclone, Logan, UT). Then cells were transferred to a sample cuvette and centrifuged at 1200 rpm at 25 °C for 5 min. The supernatant was removed, and the cell pellet was re-suspended in 400 ml of $1 \times$ ATP releasing buffer (Sigma Chemical Co., St. Louis, MO) at room temperature. Finally, 100 μl of lucigenin stock solution was added into cell lysate immediately before the reading. Lucigenin is a di-acridinium compound, which emits light on reaction with $\text{O}_2^{\bullet-}$ [19]. In our experiments, chemoluminescence was obtained after adding lucigenin to fresh cell lysate.

2.5. Ca^{2+} measurements using Fura-2 am

Cells were incubated with Fura-2 am in Ca^{2+} measurement buffer at a concentration of 5 μM for 30 min at room temperature, and then they were changed into indicator-free buffer (HBSS containing 1 mM Ca^{2+}) for 30 min for de-esterification of intracellular AM esters. After that, measurements were quantified with RF-5301PC Intracellular ion measurement system (Shimadzu corporation, Japan). When the baseline $F_{\lambda=340} / F_{\lambda=380}$ fluorescence intensity ratio between bound Ca^{2+} and free Ca^{2+} stabilized, drugs (LY30 or Thapsigargin) were added according to specified concentrations and schedules. Finally, cells were treated with 0.05% Triton X-100 for calculation of R_{\max} and treated with 100 mM EGTA (5 mM final) for calculation of R_{\min} . Intracellular free Ca^{2+} concentrations were calibrated through the formula

$$\text{Ca}^{2+} = K_d Q \frac{R - R_{\min}}{R_{\max} - R}$$

where R refers to the measured fluorescence ratio between 340 and 380 $F_{\lambda=340} / F_{\lambda=380}$, R_{\max} is the maximum fluorescence ratio (calculated through Triton X-100 treatment), R_{\min} is the minimum fluorescence ratio (calculated through EGTA treatment), K_d is the Ca^{2+} dissociation constant of the Fura-2 (which can be calculated with a known concentration Ca^{2+}), and Q is the calculated ratio of F_{\min} to F_{\max} at λ_2 (~380 nm).

2.6. Ca^{2+} measurement using spinning disk confocal microscopy (SDCM)

Cells were seeded in 8-well chambers with 25,000 cells per well, and allowed to grow for 24 h. The following day, cells were washed with warm Ca^{2+} measurement buffer and stained with 25 μ M Fluo-4-am and 250 μ M probenecid at in the Ca^{2+} buffer for 1 h at room temperature. Then, the cells were washed twice before measurement via spinning disk confocal microscopy with laser excitation at 488 nm, fluorescence emission at 520 nm. For Ca^{2+} measurements after Thapsigargin treatment, images were taken every 2 s for 6 min. For Ca^{2+} measurements after LY30 or DMSO treatment, images were taken every 15 s for 45 min. SDCM data was analysed using software developed by the Fivaz group [20].

2.7. Cell viability assays

To measure cell viability, cells were plated in 24 well plates (1×10^5 cells/well) overnight to reach 80% confluency on the next day, prior to treatment. For LY30 and TRAIL combination treatment, cells were pre-incubated with 25 μ M LY30 for 1 h and then treated with 20 ng/ml of TRAIL for 24 h. For single treatments, cells were treated either with LY30 (25 μ M) for 25 h, or with TRAIL (20 ng/ml) for 24 h, to replicate the individual parts of the combined treatment. For experiments with scavengers or inhibitors, the additional compound was added into sample wells at the concentrations specified in Section 2.3. Finally, cells were washed with $1 \times$ PBS and stained with crystal violet for 20 min. The excess crystal violet solution was washed away using distilled water. For quantification, crystal violet was dissolved in 1% SDS and shaken for 1 h before measuring absorbance at 595 nm with a Tecan microplate reader.

2.8. Bayesian modelling

The connectivity of a Bayesian network is represented by a directed graph, which consists of variables nodes, denoted by ovals (for the species concentrations) and directed edges, denoted by arrows (for the causal effects). A directed edge points from a parent node (causal variable) to a child node (effect variable). A Bayesian network model establishes a conditional probability table for each node, to quantify how it is affected by its parent nodes. A conditional probability table (CPTs) specifies a discrete probability distribution for the child variable, for each possible combination of values for its parent variables. Automated learning of Bayesian network models (to establish the edges and the CPTs) was an iterative search process in which random elements of the directed graph were modified (see Section 2.8.3), the probability tables were updated (see Section 2.8.4), while each candidate model was evaluated against the input data using a Bayesian score (see Supplementary Text). A Bayesian score measures the agreement between a model and a given input dataset, by using Bayesian inference to simulate the behaviour of the model. Our input dataset was obtained from our experiments using the normalization and discretization methods described below. The structure learning, parameter estimation, model inference, and Bayesian scoring algorithms were performed using the Bayesian network toolbox (BNT) [21,22] running on MATLAB (Mathworks, Natick, MA, USA).

2.8.1. Normalization

The levels of each measured species ($[Ca^{2+}]_c$ using Fluo-4 am, RNS using DAF, $O_2^{\bullet-}$ using DHE and lucigenin, and ROS/ H_2O_2 using DCFDA) were normalized according to the formula $C_{normalized}^i = (f_m^i - f_m^{un-ctl}) / (f_m^{ctl} - f_m^{un-ctl})$ where f_m^i represents measured fluorescence intensity of sample i , f_m^{un-ctl} represents measured fluorescence intensity in unstained and untreated control, f_m^{ctl}

represents measured fluorescence intensity in untreated control, and $C_{normalized}^i$ represents calculated normalized concentration. The normalized datasets are shown in Supplementary Fig. S3.

2.8.2. Discretization

Normalized measurements (for DCFDA, DAF, DHE and Fluo-4) were discretized into three levels to represent low, medium or high concentrations (called 1–3). The minimum and maximum values of each species were first determined and then the whole range of values was divided into 3 intervals of equal width. Numerical measurements were converted to categorical data using this process of equal width interval binning. Exogenous LY30 stimulus was also binned into 3 categories, corresponding to no incubation (0 min), brief incubation (5 or 15 min) and long incubation (30 min or longer). Supplementary Fig. S4 shows the datasets obtained by discretizing our experimental data.

2.8.3. Structure learning

Structure learning was performed to select the model with highest Bayesian score. We selected a Markov Chain Monte Carlo (MCMC) algorithm called Metropolis–Hastings (MH) to search the space of possible model structures [21]. We used the recommended parameter settings of BNT (i.e., 25 steps to take before drawing samples, and 500 samples to draw from the chain after burn-in) [21,22]. To avoid residual effects from the starting state, the process was repeated 10,000 times with random starting points. After 10,000 repeats of the structure learning search, we selected the 12 models with the highest Bayesian scores.

2.8.4. Parameter estimation

CPTs were estimated for each variable node in each network structure based on the input dataset. The parameter estimation process adjusted the probabilities in the CPTs to minimize the difference between the simulated model and the observed input data. All parameter estimation tasks employed the BNT method *learn_params_em* which uses expectation-maximization.

Further modelling methods appear in the Supplementary Text, with subsections for Model simulation via inference, Model averaging, Model extension with inhibitors, and Model extension with viability.

2.9. Statistical analysis

All experiments were performed at least three times. Numerical data have been expressed as mean \pm SD. Statistical analysis was performed using the one-tailed paired Student's *t*-test considering the variances unequal. *P* values < 0.05 were considered significant.

3. Results

3.1. Time-series measurements of $O_2^{\bullet-}$, nitric oxide, and Ca^{2+} , as candidate mediators of LY30-induced ROS

Speculating that LY30 might disrupt the electron transport chain, similar to compounds such as rotenone, we tested for an increase in mitochondrial $O_2^{\bullet-}$, which could be the source of LY30-induced ROS. Mitochondrial $O_2^{\bullet-}$ and intracellular H_2O_2 were measured using the fluorescent dyes MitoSOXTM Red (MitoSOX) for mitochondrial $O_2^{\bullet-}$, and CM- H_2 DCFDA (DCFDA) for H_2O_2 . To minimize laser-induced ROS, samples were illuminated only once and multiple samples were used for measuring multiple time-points. HeLa cells were treated with 25 μ M of LY30 for incubation periods from 5 min to 2 h, and fluorescence intensity ($n = 3$ replicates) was measured using flow cytometry. Fig. 1a shows a rapid increase of DCFDA (solid line) to 1.25-fold after 5 min of LY30 treatment, and a further increase from 1.25-fold to 1.6-fold after

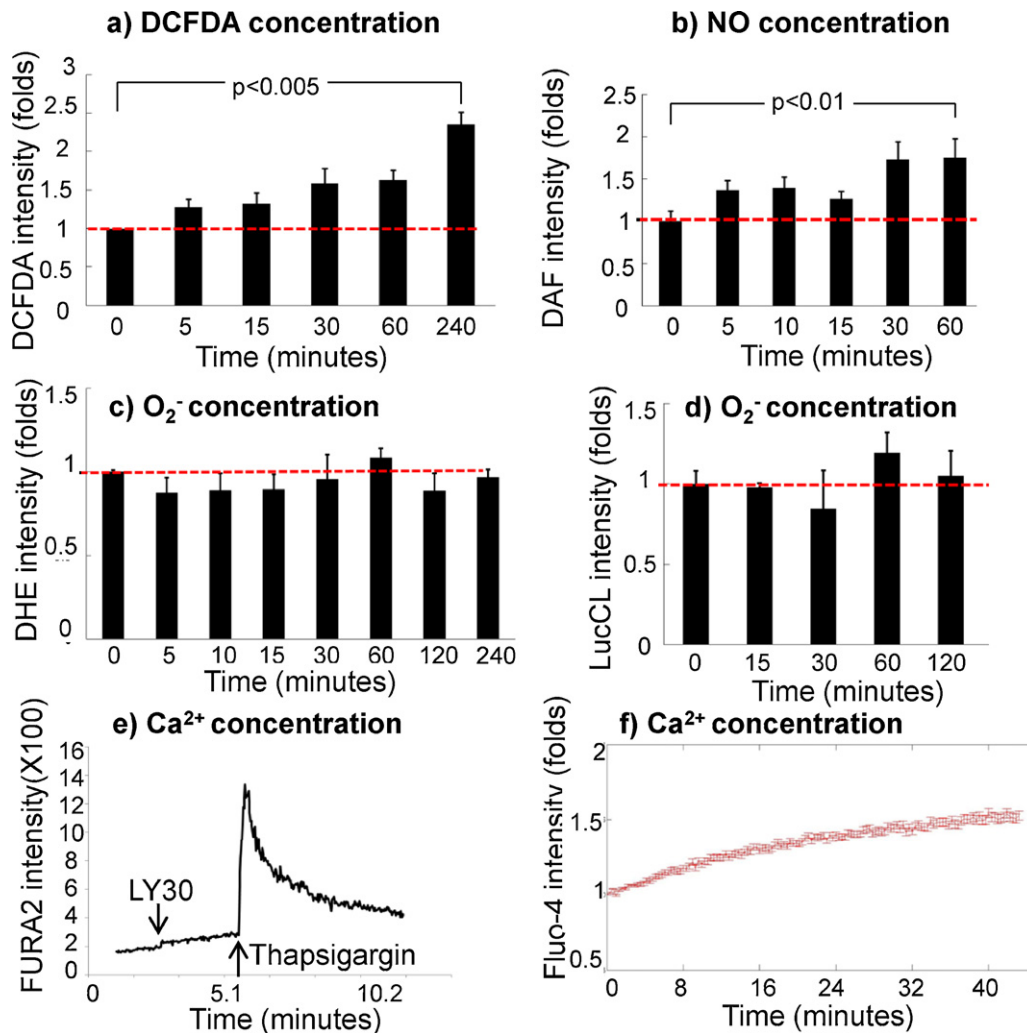


Fig. 1. Measured intensity of ROS, RNS and Ca²⁺ after LY30 treatment. For each panel, the x-axis specifies the time period of LY30 incubation in HeLa cells, and the y-axis specifies the measured fluorescence intensity for a specific dye. The fluorescence levels are plotted in units of fold-change with respect to untreated sample. (a) Measured CM-H₂DCFDA (DCFDA) fluorescence intensity levels averaged from 4 replicates. (b) Measured intensity of diamino fluorescein DAF-FM (DAF) fluorescence, from 3 replicates. Measured O₂⁻ levels using (c) dihydroethidium (DHE), or (d) lucigenin luminescence (Luc), averaged from at least 3 replicates. The changes in DHE and Luc were not statistically significant. (e) Measured levels of Ca²⁺ using radiometric dye Fura-2, for 3 replicates. (f) Measured Ca²⁺ levels using Fluo-4, averaged over a population of cells ($n > 100$).

30 min, compared with untreated control. MitoSOX dynamics (Supplementary Fig. S1c, dashed line) showed a slight increase at 15 min but no significant increase after any tested duration of LY30 treatment, from 5 min to 2 h. Cytometry of cells double-stained with DCFDA and MitoSOX also showed a sharp increase in DCFDA by 5 min and minimal effect on MitoSOX (Supplementary Fig. S1c). We conclude that mitochondrial O₂⁻ levels do not increase after LY30 treatments of up to 2 h. Mathematical simulations in Supplementary Fig. S1b shows that these experimental observations conflict with the hypothesis that LY30 causes elevated DCFDA as a result of mitochondrial O₂⁻ from disruption of the mitochondrial electron transport chain.

Other pathways, besides mitochondrial O₂⁻, that can lead to ROS production include non-mitochondrial O₂⁻ production through peroxisomes [23], NADPH oxidases 1–4 [24], or Ca²⁺-dependent activation of NADPH oxidase 5 [24]; H₂O₂ production from the endoplasmic reticulum [25]; and peroxynitrite (ONOO⁻) production from the combination of Nitric Oxide (NO) and O₂⁻ [26].

To measure total cellular O₂⁻ (instead of mitochondrial O₂⁻), we measured dihydroethidium (DHE) [27,28] and lucigenin. Neither DHE nor lucigenin showed any significant increase for LY30-treated samples of any incubation (Fig. 1b and c). The lack of

change in total O₂⁻ levels suggests that LY30 most likely has no effect on O₂⁻, but we cannot exclude the possibility that LY30 might alter both the production and consumption of O₂⁻, causing a change in the turnover rate without changing the steady state concentration.

To test for involvement of reactive nitrogen species (RNS), we used DAF-FM (DAF) [29]. Averaged DAF fluorescence, normalized to untreated control (Fig. 1d), showed a 50% increase after 5 min of LY30 incubation ($p = 0.011$). Longer incubations of LY30 caused greater DAF intensity, reaching 1.7-fold at 30 min and 2-fold at 240 min. In sum, LY30 induced significant RNS production at all time points.

To test whether LY30 perturbed intracellular Ca²⁺, we used the radiometric dye Fura-2 for free and bound Ca²⁺ [30] and the non-radiometric dye Fluo-4 am for cytosolic free calcium (Ca²⁺) [31]. In the Fura-2 experiment, HeLa cells were incubated with LY30 (25 μM) for 100 s and fluorescence intensity was monitored, before adding Thapsigargin (TG) as positive control [32]. A slight but prolonged rise in Ca²⁺ levels was seen after LY30 treatment (Fig. 1e, red arrows), prior to the expected spike induced by TG. In the Fluo-4 experiment, spinning disk confocal microscopy (SDCM) monitored Fluo-4 in single cells ($n > 100$). Tracking and quantification software

[20] extracted the Ca^{2+} dynamics (Fig. 1f), which showed a slight but prolonged Ca^{2+} increase following LY30 treatment. Positive and negative control treatments appear in Supplementary Fig. 2. We conclude that LY30 elevated Ca^{2+} but we do not know if this increase would be sufficient to trigger Ca^{2+} -induced mechanisms of ROS production, or Ca^{2+} -induced mechanisms of apoptosis sensitization.

3.2. Training a Bayesian network model of the causal linkage from LY30 to DCFDA

Bayesian probability is a mathematical framework for computing conditional probabilities, such as the probability of an effect occurring, given that a cause has been observed, Prob (Effect | Cause), or for reasoning “backwards” from effects to causes, such as the probability of a possible cause given an observed effect, Prob (Cause | Effect). Bayesian belief networks, or simply Bayesian networks, are a modelling formalism to represent causal dependencies between multiple variables in a system, provided that the variables do not exhibit any cycles of causality (i.e., circular logic). The merits and limitations of Bayesian network modelling are summarized in the discussion.

The nodes of a Bayesian network are the variables in a system, and the relationships between the variable nodes are directed edges representing causal relationships. In addition, each variable node has a conditional probability table that provides the mathematical probabilities of its possible values, given the possible combinations of its upstream (causal) variables. For further background on Bayesian networks, see [33] or the textbook [34].

We utilized Bayesian networks to represent possible networks of causality downstream of LY30 and upstream of DCFDA. The node for LY30 was constrained to be the causal “root” of the tree, upstream of all other variable nodes. The node for DCFDA was constrained to be the downstream output of the system, upstream of nothing. We selected three additional variables – $\text{O}_2^{\bullet-}$, RNS and Ca^{2+} – to be additional variable nodes in network, and we required the values of these variable nodes to be discretized into 3 states representing low, medium, and high levels of the species. The LY30 variable was divided into three possible values representing the duration of treatment: untreated, brief, and long incubation times (see Section 2). Not knowing the cause/effect relationships of

superoxide, RNS and Ca^{2+} towards each other or towards DCFDA, we did not impose any constraints on the placement or relative connectivity of the $\text{O}_2^{\bullet-}$, RNS and Ca^{2+} nodes in the network (including dead-ends with no impact on DCFDA). Instead, we used a computational strategy to search among the 12,800 possible combinations of directed edges for the whole network, using the Bayesian network toolbox (BNT) [21,22] as described in Section 2. The Bayesian score [35] was used for evaluating the agreement of each network structure with the training dataset. The training dataset (Supplementary Fig. S4) was a normalized discretization of the data in Fig. 1 (see Section 2). To avoid over-fitting with a single “highest-score” model, we selected common features through “model averaging,” an approach used for studying phosphorylation in human T cell signalling [36]. The 12 network structures with highest Bayesian scores were selected to be our candidate models (Fig. 2), and we performed parameter estimation again, to obtain refined probability values for the conditional probability tables (CPTs).

For the 12 top-scoring candidate networks, we simulated the probabilities for the RNS, Ca^{2+} , $\text{O}_2^{\bullet-}$ and DCFDA variables, under 3 conditions: no LY30 treatment, brief LY30 incubation, and long LY30 incubation. The averages of these probabilities were taken as our consensus, and plotted in Fig. 3. For example, Fig. 3 simulations show 100% probability that RNS levels would be low after no LY30 treatment, 28% probability RNS would be low and 72% probability that RNS would be medium with brief LY30 incubation, and over 90% probability that RNS would be high with long LY30 incubation. Fig. 3 consensus probabilities for the levels of RNS, Ca^{2+} , $\text{O}_2^{\bullet-}$ and DCFDA are consistent, at low resolution, with the experimental observations in Fig. 1. This indicates that our modelling has “learned” [34] the information in the training dataset, but it does not indicate whether the Bayesian modelling has predictive ability beyond the training set it was given, nor whether the causal linkages are correct.

Next we predicted the causal contribution (not the correlation) of each intermediate variable ($\text{O}_2^{\bullet-}$, RNS and Ca^{2+}) towards DCFDA fluorescence, by simulating the levels of DCFDA in the 12 top-scoring models after virtual experiments inhibiting each variable individually (blocking RNS, chelating Ca^{2+} , scavenging $\text{O}_2^{\bullet-}$, or media). For the three possible LY30 treatment durations (no

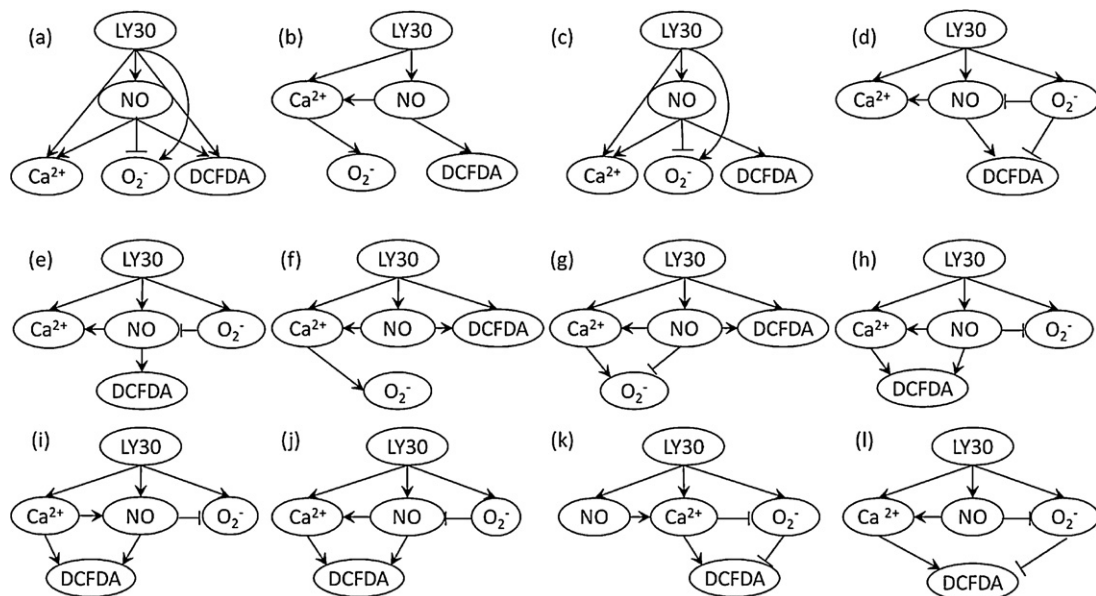


Fig. 2. The top 12 Bayesian network models describing the causal dependencies between LY30, RNS, $\text{O}_2^{\bullet-}$, free Ca^{2+} and DCFDA. Networks were generated by the structure learning algorithm, and evaluated with the Bayesian score using BNT software (see Section 2). The training dataset for the model building process was a normalized, discretized version of the data from Fig. 1 (see Supplementary Figs. S3 and S4).

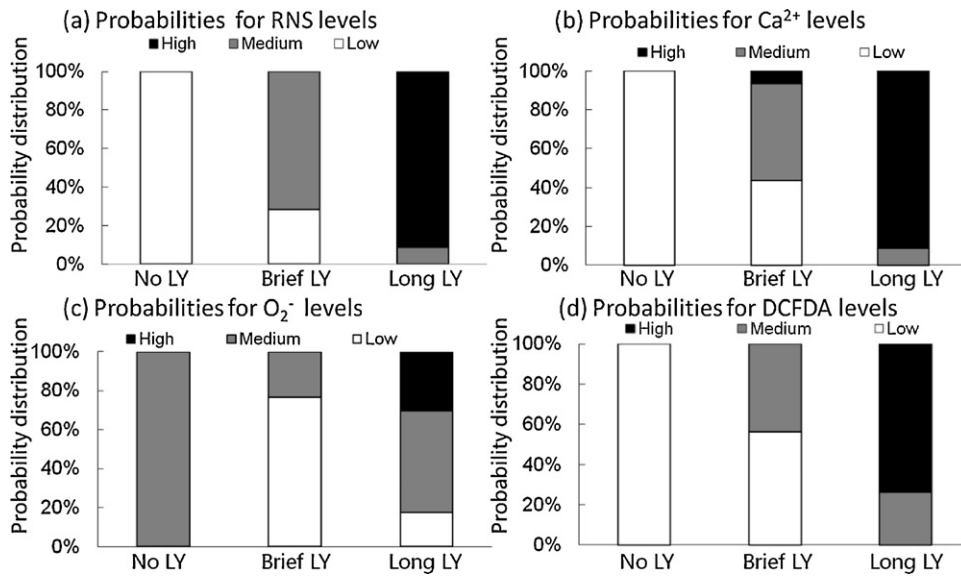


Fig. 3. Probabilities for RNS, Ca²⁺, O₂⁻ and DCFDA, averaged from the top 12 models, according to three durations of LY30 incubation. The probability that (a) the RNS level (DAF intensity), (b) the Ca²⁺ level (Fluo-4 intensity), (c) the O₂⁻ signal (Fluo-4 intensity), or (d) the DCFDA intensity will be low, medium or high, according to the duration of LY30 treatment. The information in the training dataset, originally observed as numerical signal intensities, is incorporated into the Bayesian network modelling as numerical probabilities of discrete high, medium, and low signal intensities.

(a) demonstration of probability distribution over low, medium and high with LY30 long treatment

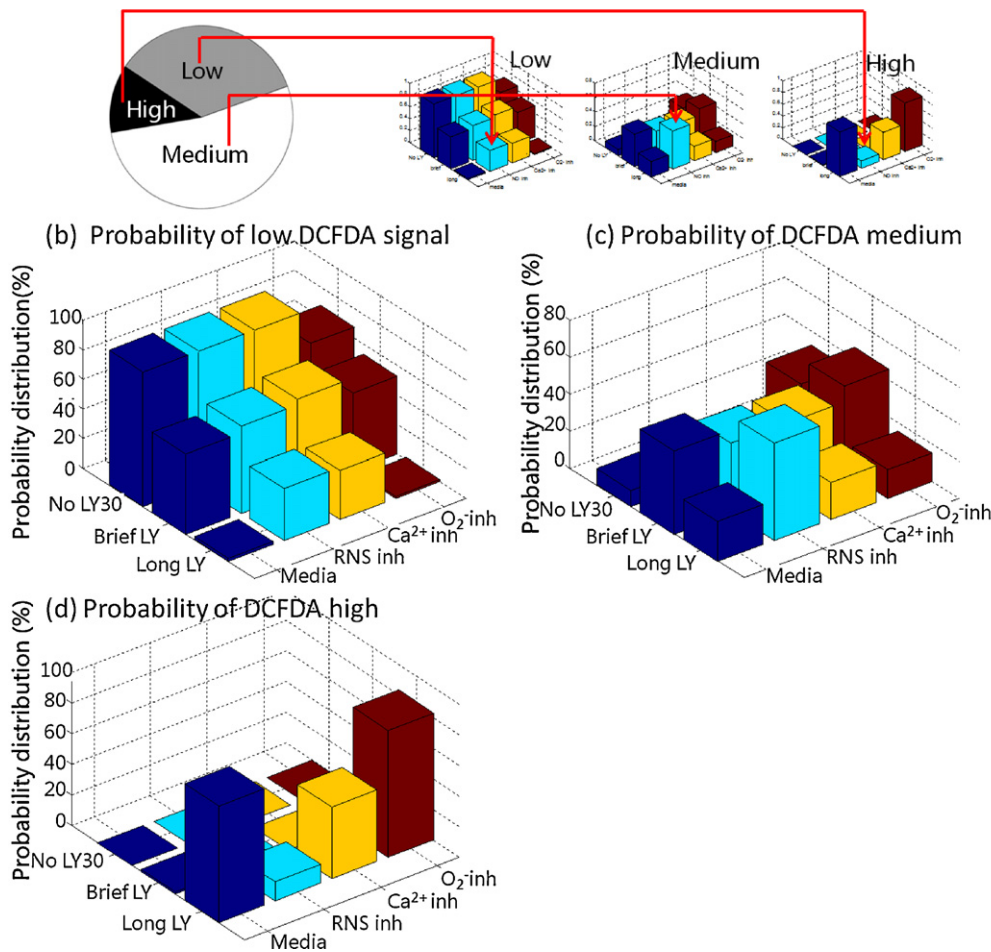


Fig. 4. The predicted intensities of DCFDA, expressed as conditional probabilities from the Bayesian networks. (a) An example of how to read tabulated probabilities is demonstrated by comparing with a familiar pie chart. The conditional probabilities for each context will always sum to 100%. The probability that DCFDA signal intensity will be (b) low, (c) medium and (d) high, was predicted by simulating the 12 top models (Fig. 2) and averaging the results. Each predicted probability (vertical axis) corresponded to a combination of LY30 treatment duration (untreated, brief, and long) and inhibitor treatment (Control media, RNS inhibitor, Ca²⁺ inhibitor, or O₂⁻ inhibitor) along the horizontal axes.

treatment, brief incubation, and long incubation), we simulated the probability of low, medium or high DCFDA levels, yielding a total of $(4 \text{ scavengers}) \times (3 \text{ incubation times}) \times (3 \text{ levels of DCFDA}) = 36$ probabilities. Fig. 4a illustrates how the Bayesian network probability distributions can be interpreted as piecharts. Fig. 4b–d shows the averaged predictions for all 12 $((4 \text{ scavengers}) \times (3 \text{ incubation times}))$ probabilities.

The most significant prediction from these probability distributions is that RNS blockage would cause the “high DCFDA” state to decrease from 75% to 12% probable (dark blue versus light blue bars in the “long incubation” row of Fig. 4d). In other words, the modelling predicted that scavenging RNS would show a strong inhibitory effect on the DCFDA signal, particularly for LY30 treatments >30 min. Note that in 10 of the 12 top-scoring models, RNS was a direct, positive mediator from LY30 to DCFDA, explaining the importance of RNS in the averaged predictions.

Another prediction from the simulations was that Ca^{2+} chelation would cause the “medium DCFDA” state to decrease from 45% to 37% under brief LY30 treatments. Finally, $\text{O}_2^{\bullet-}$ was predicted to have no significant effect on DCFDA, but interestingly, this prediction was not based on DCFDA being independent of $\text{O}_2^{\bullet-}$. Observe that 9 of the top 12 modes predicted antagonism between RNS and $\text{O}_2^{\bullet-}$ (with uncertainty about whether the antagonism was from RNS to $\text{O}_2^{\bullet-}$ or vice versa), and 4 of those 9 models predicted that the RNS– $\text{O}_2^{\bullet-}$ antagonism would be upstream of DCFDA. In sum, the modelling predicts $\text{O}_2^{\bullet-}$ to have an antagonistic relationship with NO, but little impact on DCFDA.

3.3. Testing Bayesian network predictions with scavenger/chelator experiments.

Experimental tests to determine the causal contributions of RNS, Ca^{2+} and $\text{O}_2^{\bullet-}$ to LY30-induced DCFDA were conducted using FeTPPS to scavenge ONOO⁻, EGTA-am to chelate Ca^{2+} , and Tiron to scavenge $\text{O}_2^{\bullet-}$ (Supplementary Tables S5–S7). To facilitate comparison between time-series measurements of fluorescent dyes, and simulated probabilities of discrete high/medium/low states, we constructed the following plot: the experimental observations were converted into 3 categories of LY30 treatment based on time of incubation (Fig. 5a); and the Bayesian probability distributions in Fig. 4 were heuristically converted into predicted concentrations (Fig. 5b), as explained in the figure caption. In addition, error bars were constructed for the modelled concentrations in Fig. 5b, based levels of disagreement among the top 12 models.

Experiments showed that the Ca^{2+} chelator EGTA-am was able to block the early increase in DCFDA fluorescence induced by brief LY30 incubations (from 1.5-fold to 1.2-fold with $p = 0.03$), but this

effect was not observed with long incubations. This is in agreement with the model prediction that a Ca^{2+} -dependent pathway of ROS production contributed to the initial rise in DCFDA after LY30 treatment.

The peroxynitrite scavenger FeTPPS (100 μM) decreased DCFDA fluorescence slightly for short LY30 incubations ($p = 0.048$), and very strongly for long LY30 incubations ($p = 0.03$), suggesting that ONOO⁻ is responsible for much of the DCFDA fluorescence caused by LY30, particularly at later time-points. The FeTPPS experiments agreed with the computational prediction, except for the magnitude of the effect after brief LY30 incubations.

The $\text{O}_2^{\bullet-}$ scavenger Tiron (10 mM) caused a slight decrease in DCFDA fluorescence (from 1.45-fold to 1.38-fold $p = 0.047$) for short incubations, and a significant decrease (from 1.89-fold to 1.53-fold with $p = 0.02$) for long incubations, suggesting that $\text{O}_2^{\bullet-}$ plays a causal role in LY30-induced ROS production, especially at late time points. The significant decrease of DCFDA after Tiron treatment would seem to refute the prediction that $\text{O}_2^{\bullet-}$ would not significantly affect DCFDA.

Overall, Fig. 5 and the comparison between modelling and experiments showed that Bayesian modelling was capable of reproducing the experimental effects of ONOO⁻-dependent late ROS production, and Ca^{2+} -dependent early ROS production, but it underestimated the impact of Tiron.

3.4. Cell sensitization to TRAIL-induced apoptosis

We have thus far studied LY30 effects on ROS but not on cell viability. To understand how LY30 induces HeLa cell sensitization to TRAIL-induced apoptosis, we measured cell viability after LY30 + TRAIL treatment, in cells that had been pre-treated with one of the following scavengers/inhibitors: FeTPPS, EGTA-am, Tiron, DDC, or catalase (Fig. 6). DDC is an inhibitor of SOD (superoxide dismutase), and it causes increased $\text{O}_2^{\bullet-}$ accumulation. Catalase is an antioxidant enzyme that specifically scavenges H_2O_2 , and extracellular catalase can lower intracellular H_2O_2 levels because H_2O_2 is membrane permeable.

HeLa cells treated with LY30 + TRAIL exhibited 40% viability, compared with untreated HeLa (100% viability). Pre-treatment with FeTPPS (100 μM) improved cell viability from 40% to 65% (25% rescue with $p = 0.0063$), and the inactive analogue FeCl_3 had no effect (Supplementary Fig. S3), suggesting an essential role for ONOO⁻ in LY30-induced sensitization to apoptosis. Quantified cell viability showed that EGTA-am, Tiron and DDC were also able to rescue cell death significantly (18%, 20% and 28%, respectively). Interestingly, catalase did not cause significant rescue of cell death, so we measured whether catalase decreased LY30-induced ROS

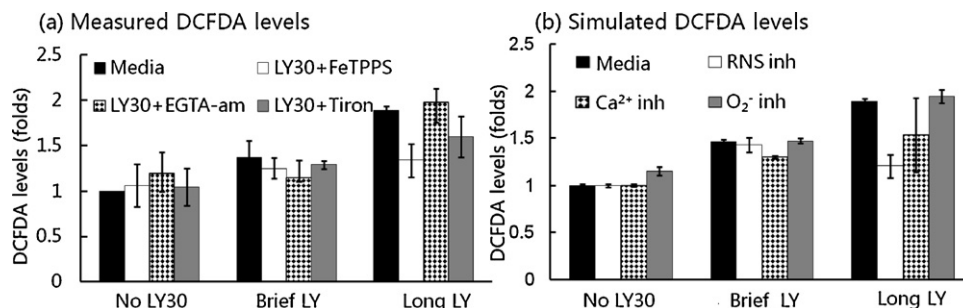


Fig. 5. Comparison between simulated DCFDA and measured DCFDA, for scavenger/chelator experiments. (a) DCFDA intensity was measured after HeLa were treated with various scavenger/chelator compounds plus LY30. Tiron was used as $\text{O}_2^{\bullet-}$ scavenger. (b) The probability distribution of DCFDA from Fig. 4 has been plotted as fold-change relative to untreated control. The predicted probability distributions of DCFDA at low, medium and high levels have been converted into absolute concentration using the formula $\text{DCFDA}_{\text{averaged}} = 0.1 \times \text{DCFDA}_{\text{averaged}}^1 + 0.4 \times \text{DCFDA}_{\text{averaged}}^2 + 0.9 \times \text{DCFDA}_{\text{averaged}}^3$, where $\text{DCFDA}_{\text{averaged}}^1$, $\text{DCFDA}_{\text{averaged}}^2$ and $\text{DCFDA}_{\text{averaged}}^3$ represented averaged probability distributions of DCFDA at low, medium and high levels, respectively. $\text{DCFDA}_{\text{averaged}}$ is the absolute DCFDA level after conversion, and it is then normalized to the calculated DCFDA levels for untreated control. The error bars represent standard deviations for each average of the top 12 models.

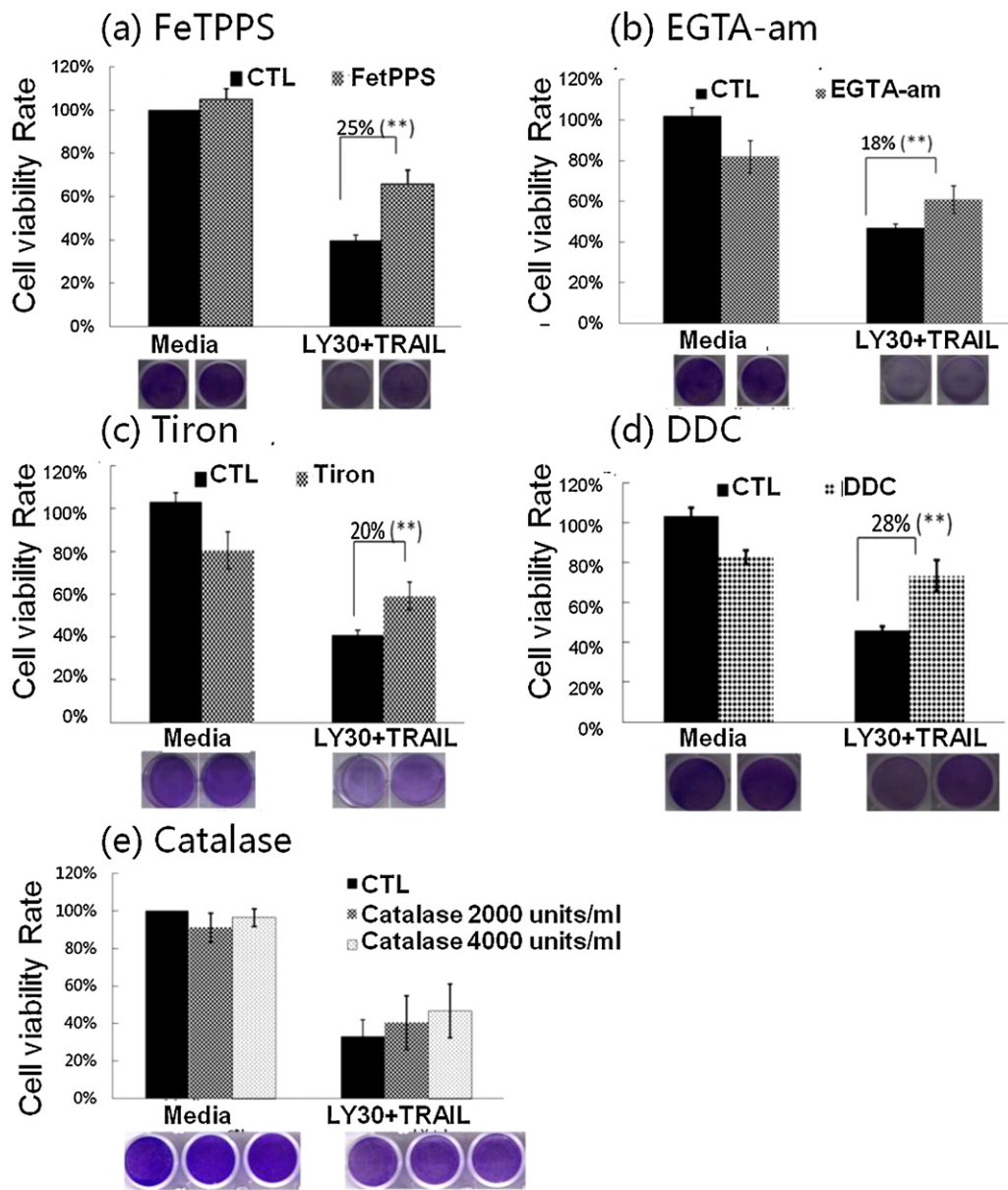


Fig. 6. Cell viability of HeLa cells after LY30 \pm TRAIL treatment, in the presence of scavenger/chelator compounds. Cell viability (a) with/without FeTPPS (100 μ M), (b) with/without EGTA-am (50 μ M), (c) with/without Tiron (10 mM), (d) with/without DDC (200 μ M), (e) with/without catalase 2000 units/ml or 4000 units/ml.

(Supplementary Fig. S4). Catalase suppressed a significant fraction of DCFDA fluorescence induced by 5 min of LY30 treatment, but it had no significant impact on the DCFDA levels induced by longer incubations of LY30. This suggests that H_2O_2 is not a significant fraction of LY30-induced ROS in HeLa, except at very early time points.

To represent our best current understanding of LY30 effects in HeLa, the Bayesian modelling consensus from Figs. 3 and 4 was extended as follows. The consensus links between RNS, $O_2^{\bullet-}$, Ca^{2+} and DCFDA were retained (depicted as straight, solid lines in Fig. 7a), and RNS was renamed nitric oxide (NO) because its training data came from the NO-specific dye DAF. New variable nodes were created for $ONOO^-$, H_2O_2 , and cell sensitization to TRAIL (“Sensit”). Then, to connect the new variables with the network, possible pathways (dotted arcs in Fig. 7a) were added manually based on published literature. Directed edges were inserted from $O_2^{\bullet-}$ and NO to the $ONOO^-$ variable node because $O_2^{\bullet-}$ and NO react strongly to produce $ONOO^-$. Additional “dotted” arrows were added from Ca^{2+} to H_2O_2 [24,37], from $O_2^{\bullet-}$ to H_2O_2

[38,39], and from most of the species to apoptosis sensitization. Finally, exogenous binary variables (present/absent) were created for the inhibitors FeTPPS, EGTA-am, Tiron, DDC, and catalase. Negative influences were added for FeTPPS towards $ONOO^-$, for EGTA-am towards Ca^{2+} , and for catalase towards H_2O_2 . The obvious effect of DDC on superoxide was added, as well as the published side-effect that DDC can suppress NO levels. A negative effect of Tiron on superoxide was added, along with the published side-effect that Tiron can decrease $ONOO^-$. The “exogenous” variables (the inhibitors and scavengers) and their causal links are shaded grey in Fig. 7a.

Starting with the network connectivity in Fig. 7a, we used the expectation-maximization algorithm to estimate the causal contributions of the dotted arrows by optimizing the fit between the model and the experimental data. The exogenous effects (grey arrows) were not adjusted. The training dataset for the parameter estimation was the cell viability data from Fig. 6. The Supplementary Text provides complete information for the construction of the extended model with viability.

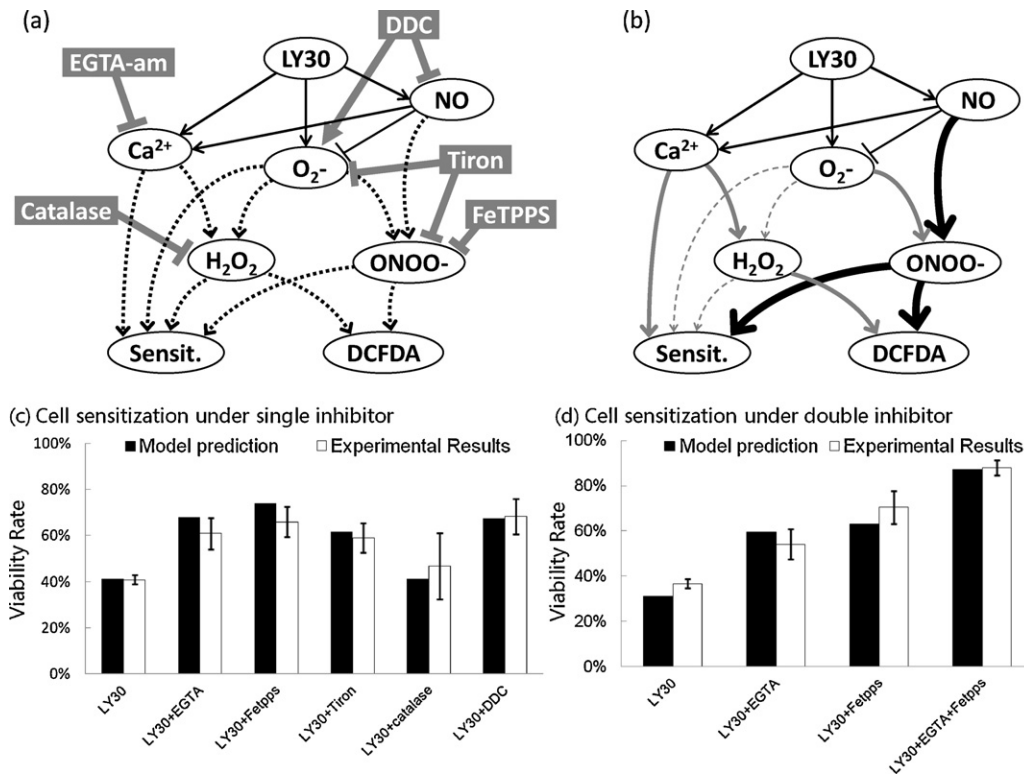


Fig. 7. Modelling Cell sensitization to TRAIL. (a) An initial network structure was generated using the consensus links of Fig. 2 (straight solid lines), adding additional variable nodes, and creating hypothetical edges (dashed arcs) based on published literature. (b) Conditional probability tables were generated by the BNT software (parameter estimation algorithm) using cell viability as the training dataset. The result is an extended model. The causal linkages in the conditional probability tables of the extended model have been summarized in the shading of the curved edges: thick black arrows for strong effects, grey arrows for moderate effects, and thin dashed edges for negligible effects. (c) Comparison of cell viability results from the extended model and from the experiments, to assess whether the model can recapitulate the training dataset. Black bars represent simulated cell viabilities and grey bars represent experimentally observed viability. (d) Cell viability prediction for a separate independent test, and experimental confirmation of the prediction. For the single and double inhibitor treatments, HeLa cells were incubated with FeTPPS (100 μ M) for 1 h before adding LY30, and/or with EGTA-am (25 μ M) for 15 min before adding LY30.

The resulting model (Fig. 7b) shows the literature-based effects, shaded according to computed strength of causation: thick black lines for strong causation, grey lines for moderate causation, and thin dashed lines for insignificant causation. This network serves as an automated interpretation of likely mechanisms, corresponding to our experimental observations. Fig. 7c shows that the extended model was able to recapitulate the experimental results in the training set, as expected. Finally we sought to compare the model against a separate test. The model was simulated, for each possible pair of scavenger/inhibitor compounds, plus LY30 and TRAIL, to obtain predictions of cell sensitization with scavenger combinations (Supplementary Fig. S5). The results predict that combining EGTA-am and FeTPPS would cause the greatest rescue of cell death. We conducted a cell viability assay with FeTPPS and EGTA-am, together with LY30 and TRAIL. As shown in Fig. 7d, the predicted cell viability showed close agreement with the observed viability.

4. Discussion

Previous literature on cell stress signalling has elucidated many causal linkages between Ca²⁺, various species of ROS, and various species of RNS, yielding countless possible pathways downstream of LY30 to mediate cell sensitization to apoptosis. We chose Bayesian networks to model LY30-induced effects for several reasons. Firstly, the directed edges in Bayesian networks are a flexible architecture to permit fast generation and testing of many hypotheses about connectivity. Secondly, the predictions derived with a Bayesian model are qualitative and thus are less sensitive to changes in parameter values [40]. Thirdly, statistically insignificant changes in observed variables can be represented

as low-probability changes in a Bayesian network variable (rather than being ignored); this flexibility allows evidence from many minor correlations to accumulate mathematically into a significant net effect. This third benefit explains why the Bayesian network modelling was able to infer an antagonistic relationship between NO and O₂⁻ (Fig. 2), simply based on inverse correlations in the time series trends, and not based on any prior knowledge of chemistry.

A crucial weakness of Bayesian network modelling is that it cannot represent feedback loops or cycles of causality. The species studied in this project are highly interdependent and likely to participate in feedback loops. Feedback mechanisms have been excluded from our analysis, due to our choice of Bayesian network formalism, and we do not know how feedback would impact the analysis. Another weakness of our approach is vulnerability to discretization effects, which can flatten important information, or amplify random noise, depending on the arbitrary boundaries of the high/medium/low categories. Our “equal width interval binning” method of discretization caused artificial amplification of the O₂⁻ fluctuations (Supplementary Fig. S4). The O₂⁻ fluctuations likely aided in detecting the negative correlation between NO and O₂⁻, but this amplification of a “flat” signal could have been harmful in another context.

Bayesian modelling analysed time series observations of correlational experiments (without any mechanistic perturbations), and yielded predictions for the causal contributions of RNS, Ca, and O₂⁻ to LY30-induced DCFDA fluorescence. Blocking RNS was predicted to suppress DCFDA induction, especially for LY30 treatments ≥ 30 min. Seeking biological mechanisms that could be responsible for such an effect, we speculate that RNS could affect

DCFDA because NO can lead to production of ONOO⁻ [41,42], which is an effective trigger for DCFDA fluorescence [41,42]. Indeed this mechanism is consistent with the “test set” experiment, in which the ONOO⁻ scavenger FeTPPS caused >80% decrease in LY30-induced DCFDA fluorescence, for long incubation times.

Another prediction from the Bayesian modelling was that chelation of Ca²⁺ would have some inhibitory effect on LY30-induced DCFDA fluorescence. For brief LY30 incubations, this prediction had high confidence (small error bar in Fig. 5b), but for simulations of long incubations, the top-12 models exhibited unusually large disagreement. The test-set experiment with EGTA-am validated the importance of Ca²⁺ for early induction of DCFDA. In theory, Ca²⁺ could affect DCFDA through the mitochondrial pathway, but the low MitoSOX readings in Fig. 1 make that less likely. We speculate that the mechanism for the observed effects of Ca²⁺ might be direct production of H₂O₂ through Ca²⁺-dependent NOX5 activation [24].

The third prediction from the Bayesian modelling was that LY30-induced ROS was not mediated by O₂^{•-}. This prediction is exceedingly intuitive and would seem obvious, given the series of experiments showing that LY30 did not increase O₂^{•-} levels. Remarkably, Tiron treatment to scavenge O₂^{•-} [43] did cause a significant decrease in DCFDA (Fig. 5) and significant improvement in cell viability (Fig. 6). One possible interpretation is that normal concentrations of O₂^{•-}, which are in excess of NO [26], allowed LY30-induced NO to react with O₂^{•-} to produce ONOO⁻, but removing O₂^{•-} prevented the LY30-induced NO from making ONOO⁻. Multiple previous studies have found Tiron to decrease apparent ONOO⁻ levels and similar mechanisms have been observed with another SOD mimetic, Tempol [44]. This scenario, in which ONOO⁻ mediates the impact of Tiron, is not falsified by the observation of constant O₂^{•-} levels after LY30 treatment, because LY30 could in theory increase O₂^{•-} production at approximately the same rate that LY30-induced NO depletes the additional O₂^{•-}. Another different interpretation is that Ca²⁺ instead of O₂^{•-} might have mediated the effects of Tiron. Tiron has been shown to bind Ca²⁺ [45] and we know that DCFDA levels are sensitive to Ca²⁺ in this context. We can conclude that Tiron significantly suppresses LY30-induced effects, but we cannot conclude whether some of this effect is mediated by ONOO⁻ or other effects besides O₂^{•-}.

The mechanisms by which LY30 sensitizes HeLa to TRAIL-induced apoptosis were probed by measuring cell viability after LY30 + TRAIL, with and without scavengers/chelators for potential mediators of the sensitization. ONOO⁻ can cause cellular damage and necrosis, but low levels can lead to nitrosative stress and apoptotic death [14], which may be a promising avenue for future cancer therapies [46]. ONOO⁻ is more reactive than H₂O₂, NO, or O₂^{•-}, and low levels of ONOO⁻ can activate DCFDA fluorescence very potently [41]. In our LY30 experiments, scavenging ONOO⁻ caused a very strong rescue of DCFDA fluorescence, and a very strong rescue of HeLa viability after TRAIL treatment (Fig. 6). We conclude that ONOO⁻ is a central mediator of LY30-induced effects, both ROS and apoptosis sensitization.

Other perturbations were also able to rescue cell viability, such as EGTA-am to chelate Ca²⁺. A causal effect of Ca²⁺ towards apoptosis sensitization is consistent with the importance of Ca²⁺ as a mediator of LY30-induced ROS, which was confirmed in Fig. 5. The extended model with cell viability (Fig. 7) inferred that Ca²⁺ has a significant causal effect on H₂O₂. Future work should test whether LY30-induced Ca²⁺ can produce H₂O₂ directly, for example through NOX5 [24].

More surprising were the results with DDC to block conversion of O₂^{•-} into H₂O₂, and Tiron to scavenge O₂^{•-} and accelerate conversion into H₂O₂. Because DDC and Tiron promote opposite O₂^{•-} effects (decreasing or increasing

conversion into H₂O₂), it is puzzling that both these treatments had the same effect, blocking sensitization to apoptosis. Another puzzle is why modulators of O₂^{•-} would have any impact on the effects of LY30, given that LY30 treatment caused no significant change in O₂^{•-} levels. In the discussion of the DCFDA experiments, we interpreted the Tiron effects either as a non-canonical effect on Ca²⁺, or as creating a new bottleneck at O₂^{•-} availability which limited production of ONOO⁻. Both interpretations are plausible explanations for the effect of Tiron on cell viability. The impact of DDC on cell viability could be mediated by O₂^{•-}, or by off-target effects of the DDC inhibitor. O₂^{•-} has potent anti-apoptotic effects [47], and elevation of O₂^{•-} could plausibly explain the rescue of cells by DDC treatment. Alternatively, DDC can reduce intracellular NO by inhibiting inducible NO synthase (iNOS) [48,49]. If DDC suppresses NO in LY30-treated HeLa, then DDC could block LY30 effects by blocking ONOO⁻ production, rather than through increased superoxide. Computational modelling selected NO suppression as most likely for the extended model in Fig. 7b. Future work should confirm whether O₂^{•-} truly mediates the effects of Tiron and DDC on the apoptosis sensitization of LY30, or whether off-target effects on Ca²⁺ and NO are responsible.

DCFDA was once thought to be specific for H₂O₂ [50], but is now understood as a more general marker of ROS. DCFDA experiments with catalase showed that LY30 did cause H₂O₂ production at early time points (Supplementary Fig. S6), but much of LY30-induced DCFDA fluorescence was not H₂O₂ (i.e., not affected by catalase). To ascertain the involvement of H₂O₂ in LY30-induced cell sensitization, we tested whether catalase blocked cell death after treatment with LY30 + TRAIL. Catalase at 2000 units/ml and 4000 units/ml showed little rescue of cell viability (Fig. 6e), indicating that H₂O₂ is not responsible for LY30-induced sensitization to TRAIL in HeLa. Since H₂O₂ has exhibited consistently pro-apoptotic effects in diverse contexts [51], we are led to speculate that LY30-induced H₂O₂ might be having some degree of pro-apoptotic effects in HeLa, but the downstream impact of H₂O₂ on viability could be masked in HeLa by the faster apoptotic effects of ONOO⁻.

Previous work found that catalase blocked LY30-induced sensitization of LnCaP cells to vincristine-induced apoptosis [3], and blocked LY30-induced sensitization of SHEP-1 neuroblastoma cells to TRAIL-induced apoptosis [5], but did *not* block sensitization of HeLa to TRAIL-induced apoptosis [4]. Different cellular capacities to produce NO and RNS might explain the observed cell type differences in the importance of H₂O₂ versus ONOO⁻ for cell sensitization. Neuroblastoma cells have low levels of iNOS [52], and we speculate that LY30 induces more NO production in HeLa than in SHEP-1. In HeLa, high NO levels would cause more ONOO⁻ and more peroxynitrite-dependent death. This effect would be compounded if HeLa cells are more sensitive to NO than other cell types, as previously reported [53]. Future work should compare the expression levels of NOS and NOX isoforms in different types of cancer, to understand differential regulation of apoptosis sensitization. Our experimental and computational findings agree that LY30 triggers several pathways of stress, moving cancer cells closer to apoptosis by multiple simultaneous mechanisms. In these highly primed contexts, the “final straw” that causes death may be a small increase in a reactive species or a second messenger, and the final apoptotic outcome may depend on protein levels and cell types.

Appendix A. Supplementary data

Supplementary data associated with this article can be found, in the online version, at <http://dx.doi.org/10.1016/j.bcp.2012.08.028>.

References

- [1] Jacobs MD, Black J, Futer O, Swenson L, Hare B, Fleming M, et al. Pim-1 ligand-bound structures reveal the mechanism of serine/threonine kinase inhibition by LY294002. *J Biol Chem* 2005;280:13728–34.
- [2] Gharbi SI, Zvelebil MJ, Shuttleworth SJ, Hancox T, Saghir N, Timms JF, et al. Exploring the specificity of the PI3K family inhibitor LY294002. *Biochem J* 2007;404:15–21.
- [3] Poh TW, Pervaiz S. LY294002 and LY303511 sensitize tumor cells to drug-induced apoptosis via intracellular hydrogen peroxide production independent of the phosphoinositide 3-kinase-Akt pathway. *Cancer Res* 2005;65:6264–74.
- [4] Poh TW, Huang S, Hirpara JL, Pervaiz S. LY303511 amplifies TRAIL-induced apoptosis in tumor cells by enhancing DR5 oligomerization, DISC assembly, and mitochondrial permeabilization. *Cell Death Differ* 2007;14:1813–25.
- [5] Shenoy K, Wu Y, Pervaiz S. LY303511 enhances TRAIL sensitivity of SHEP-1 neuroblastoma cells via hydrogen peroxide-mediated mitogen-activated protein kinase activation and up-regulation of death receptors. *Cancer Res* 2009;69:1941–50.
- [6] Zhang L, Fang B. Mechanisms of resistance to TRAIL-induced apoptosis in cancer. *Cancer Gene Ther* 2005;12:228–37.
- [7] Mellier G, Huang S, Shenoy K, Pervaiz S. TRAILing death in cancer. *Mol Aspects Med* 2010;31:93–112.
- [8] Simizu S, Takada M, Umezawa K, Imoto M. Requirement of caspase-3(-like) protease-mediated hydrogen peroxide production for apoptosis induced by various anticancer drugs. *J Biol Chem* 1998;273:26900–07.
- [9] Huang HL, Fang LW, Lu SP, Chou CK, Luh TY, Lai MZ. DNA-damaging reagents induce apoptosis through reactive oxygen species-dependent Fas aggregation. *Oncogene* 2003;22:8168–77.
- [10] Trachootham D, Zhou Y, Zhang H, Demizu Y, Chen Z, Pelicano H, et al. Selective killing of oncogenically transformed cells through a ROS-mediated mechanism by beta-phenylethyl isothiocyanate. *Cancer Cell* 2006;10:241–52.
- [11] Apel K, Hirt H. Reactive oxygen species: metabolism, oxidative stress, and signal transduction. *Annu Rev Plant Biol* 2004;55:373–99.
- [12] Pervaiz S, Clement M-V. Superoxide anion: oncogenic reactive oxygen species? *Int J Biochem Cell Biol* 2007;39:1297–304.
- [13] Hidalgo C, Donoso P. Crosstalk between calcium and redox signaling: from molecular mechanisms to health implications. *Antioxid Redox Signaling* 2008;10:1275–312.
- [14] Virág L, Szabó E, Gergely P, Szabó C. Peroxynitrite-induced cytotoxicity: mechanism and opportunities for intervention. *Toxicol Lett* 2003;141:113–24.
- [15] Brown GC. Regulation of mitochondrial respiration by nitric oxide inhibition of cytochrome c oxidase. *Biochim Biophys Acta* 2001;1504:46–57.
- [16] Yan Y, Wei C-liang, Zhang W-rui, Cheng H-ping, Liu J. Cross-talk between calcium and reactive oxygen species signaling. *Acta Pharmacol Sin* 2006;27:821–6.
- [17] Bánfi B, Molnár G, Maturana A, Steger K, Hegedűs B, Demareux N, et al. A Ca(2+)-activated NADPH oxidase in testis, spleen, and lymph nodes. *J Biol Chem* 2001;276:37594–601.
- [18] Heckerman D, Wellman MP. Bayesian networks. *Commun ACM* 1995;38:27–30.
- [19] Afanas'ev IB. Lucigenin chemiluminescence assay for superoxide detection. *Circ Res* 2001;89:E46.
- [20] Wong LC, Lu B, Tan KW, Fivaz M. Fully-automated image processing software to analyze calcium traces in populations of single cells. *Cell Calcium* 2010;48:270–4.
- [21] Murphy KP. The Bayes Net Toolbox for Matlab. In: *Computing Science and Statistics: Proceedings of the Interface*, vol. 33; 2001.
- [22] Francois O. BNT structure learning package: documentation and experiments. Technical Report FRE CNRS 2645. Laboratoire PSI, Université et INSA de Rouen; 2004.
- [23] Yeldandi AV, Rao MS, Reddy JK. Hydrogen peroxide generation in peroxisome proliferator-induced oncogenesis. *Mutat Res* 2000;448:159–77.
- [24] Bedard K, Krause KH. The NOX family of ROS-generating NADPH oxidases: physiology and pathophysiology. *Physiol Rev* 2007;87:245–313.
- [25] Chance B, Sies H, Boveris A. Hydroperoxide metabolism in mammalian organs. *Physiol Rev* 1979;59:527–605.
- [26] Beckman JS, Koppenol WH. Nitric oxide, superoxide, and peroxynitrite: the good, the bad, and ugly. *Am J Physiol* 1996;271:C1424–37.
- [27] Bindokas VP, Jordan J, Lee CC, Miller RJ. Superoxide production in rat hippocampal neurons: selective imaging with hydroethidine. *J Neurosci* 1996;16:1324–36.
- [28] Li N, Ragheb K, Lawler G, Sturgis J, Rajwa B, Melendez JA, et al. Mitochondrial complex I inhibitor rotenone induces apoptosis through enhancing mitochondrial reactive oxygen species production. *J Biol Chem* 2003;278:8516–25.
- [29] Kojima H, Sakurai K, Kikuchi K, Kawahara S, Kirino Y, Nagoshi H, et al. Development of a fluorescent indicator for nitric oxide based on the fluorescein chromophore. *Chem Pharm Bull (Tokyo)* 1998;46:373–5.
- [30] Grynkiewicz G, Poenie M, Tsien RY. A new generation of Ca²⁺ indicators with greatly improved fluorescence properties. *J Biol Chem* 1985;260:3440–50.
- [31] Gee KR, Brown KA, Chen WN, Bishop-Stewart J, Gray D, Johnson I. Chemical and physiological characterization of fluo-4 Ca(2+)-indicator dyes. *Cell Calcium* 2000;27:97–106.
- [32] Lytton J, Westlin M, Hanley MR. Thapsigargin inhibits the sarcoplasmic or endoplasmic reticulum Ca-ATPase family of calcium pumps. *J Biol Chem* 1991;266:17067–71.
- [33] Pearl J. Probabilistic reasoning in intelligent systems: Networks of plausible inference. San Francisco, CA, USA: Morgan Kaufmann; 1988.
- [34] Russel S, Norvig P. Artificial intelligence: A modern approach. Upper Saddle River, NJ, USA: Prentice Hall; 2009.
- [35] Sachs K. Bayesian network models of biological signaling pathways. PhD thesis. Massachusetts Institute of Technology; 2006.
- [36] Sachs K, Perez O, Pe'er D, Lauffenburger DA, Nolan GP. Causal protein-signaling networks derived from multiparameter single-cell data. *Science* 2005;308:523–9.
- [37] González A, Cabrera M, Henríquez MJ, Contreras RA, Morales B, Moenne A. Cross talk among calcium, hydrogen peroxide, and nitric oxide and activation of gene expression involving calmodulins and calcium-dependent protein kinases in *Ulva compressa* exposed to copper excess. *Plant Physiol* 2012;158:1451–62.
- [38] Kellogg EW, Fridovich I. Superoxide, hydrogen peroxide, and singlet oxygen in lipid peroxidation by a xanthine oxidase system. *J Biol Chem* 1975;250:8812–7.
- [39] Halliwell B. Generation of hydrogen peroxide, superoxide and hydroxyl radicals during the oxidation of dihydroxyfumaric acid by peroxidase. *Biochem J* 1977;163:441–8.
- [40] Samaga R, Saez-Rodriguez J, Alexopoulos LG, Sorger PK, Klamt S. The logic of EGFR/Erbb signaling: theoretical properties and analysis of high-throughput data. *PLoS Comput Biol* 2009;5:e1000438.
- [41] Possel H, Noack H, Augustin W, Keilhoff G, Wolf G. 2,7-Dihydrodichlorofluorescein diacetate as a fluorescent marker for peroxynitrite formation. *FEBS Lett* 1997;416:175–8.
- [42] Szabo C, Ischiropoulos H, Radi R. Peroxynitrite: biochemistry, pathophysiology and development of therapeutics. *Nat Rev Drug Discovery* 2007;6:662–80.
- [43] Ledenev AN, Konstantinov AA, Popova E, Ruuge EK. A simple assay of the superoxide generation rate with Tiron as an EPR-visible radical scavenger. *Biochem Int* 1986;13:391–6.
- [44] Weiss RH, Flickinger AG, Rivers WJ, Hardy MM, Aston KW, Ryan US, et al. Evaluation of activity of putative superoxide dismutase mimics. Direct analysis by stopped-flow kinetics. *J Biol Chem* 1993;268:23049–54.
- [45] Ghosh M, Wang HD, McNeill JR. Tiron exerts effects unrelated to its role as a scavenger of superoxide anion: effects on calcium binding and vascular responses. *Can J Physiol Pharmacol* 2002;80:755–60.
- [46] Hirst DG, Robson T. Nitrosative stress as a mediator of apoptosis: implications for cancer therapy. *Curr Pharm Des* 2010;16:45–55.
- [47] Clément MV, Pervaiz S. Intracellular superoxide and hydrogen peroxide concentrations: a critical balance that determines survival or death. *Redox Rep* 2001;6:211–4.
- [48] Mulsch A, Schray-Utz B, Mordvintsev PI, Hauschildt S, Busse R. Diethyldithiocarbamate inhibits induction of macrophage NO synthase. *FEBS Lett* 1993;321:215–8.
- [49] Li DX, Wang SL, Ito Y, Zhang JH, Wu CF. Diethyldithiocarbamate inhibits iNOS expression in human lens epithelial cells stimulated by IFN-gamma and LPS. *Acta Pharmacol Sin* 2005;26:359–63.
- [50] Keston AS, Brandt R. The fluorometric analysis of ultramicro quantities of hydrogen peroxide. *Anal Biochem* 1965;11:1–5.
- [51] Ahmad KA, Iskandar KB, Hirpara JL, Clement M-V, Pervaiz S. Hydrogen peroxide-mediated cytosolic acidification is a signal for mitochondrial translocation of Bax during drug-induced apoptosis of tumor cells. *Cancer Res* 2004;64:7867–78.
- [52] Huerta S, Chilka S, Bonavida B. Nitric oxide donors: novel cancer therapeutics. *Int J Oncol* 2008;33:909–27 [review].
- [53] Gil'iano Ni Bondarev GN, Konevega LV, Semenova EG, Noskin LA. [Modification of cellular radiosensitivity by NO-synthase inhibitors]. *Radiats Biol Radioecol/Rossiiskaia Akademiia Nauk* 2005;45:63–7.